Region-Enhanced Passive Radar Imaging

Müjdat Çetin and Aaron D. Lanterman

This work was supported in part by the U.S. Air Force Office of Scientific Research (AFOSR) under Grant F49620-00-0362, and the U.S. Defense Advanced Research Projects Agency (DARPA) under Grant F49620-98-1-0498.

M. Çetin is with the Laboratory for Information and Decision Systems, Massachusetts Institute of Technology, Cambridge, MA 02139, USA (e-mail: mcetin@mit.edu).

Aaron D. Lanterman is with the School of Electrical and Computer Engineering, Georgia Institute of Technology, Mail Code 0250, Atlanta, GA 30332, USA (e-mail: lanterma@ece.gatech.edu).

Abstract

We adapt and apply a recently-developed region-enhanced synthetic aperture radar (SAR) image reconstruction technique to the problem of passive radar imaging. One goal in passive radar imaging is to form images of aircraft using signals transmitted by commercial radio and television stations that are reflected from the objects of interest. This involves reconstructing an image from sparse samples of its Fourier transform. Due to the sparse nature of the aperture, a conventional image formation approach based on direct Fourier transformation results in quite dramatic artifacts in the image, as compared to the case of active SAR imaging. The region-enhanced image formation method we consider is based on an explicit mathematical model of the observation process; hence, information about the nature of the aperture is explicitly taken into account in image formation. Furthermore, this framework allows the incorporation of prior information or constraints about the scene being imaged, which makes it possible to compensate for the limitations of the sparse apertures involved in passive radar imaging. As a result, conventional imaging artifacts, such as sidelobes, can be alleviated. Our experimental results using data based on electromagnetic simulations demonstrate that this is a promising strategy for passive radar imaging, exhibiting significant suppression of artifacts, preservation of imaged object features, and robustness to measurement noise.

Keywords

Passive radar, multistatic radar, sparse-aperture imaging, image reconstruction, feature-enhanced imaging.

I. Introduction

Traditional synthetic aperture radar (SAR) systems transmit waveforms and deduce information about targets by measuring and analyzing the reflected signals.[1] The active nature of such radars can be problematic in military scenarios since the transmission reveals both the existence and the location of the transmitter. An alternative approach is to exploit "illuminators of opportunity" such as commercial television and FM radio broadcasts. Such passive approaches offer numerous advantages. The overall system cost may be cheaper, since a transmitter is no longer needed. Commercial transmitters are typically much higher in elevation than the prevailing terrain, yielding coverage of low altitude targets. Most importantly, such a system may remain covert, yielding increased survivability and robustness against deliberate directional interference. Such passive multistatic radar

[1]Ground-based systems looking at airborne targets are generally referred to as inverse SAR (ISAR); for brevity we just use the term SAR.

systems, such as Lockheed Martin's Silent Sentry, have been developed to detect and track aircraft. If one could additionally form images from such data, that would be useful in identifying the observed aircraft through image-based target recognition. This provides an alternative to the radar cross section signature-based automatic target recognition (ATR) method proposed in [1]. Imaging methods are of interest in their own right beyond the ATR application, since a system may encounter targets that are not present in the ATR system's library; in such cases, it would be good to have an image to present to a human analyst. Recently there has been some interest in image reconstruction from passive radar data. In particular, [2] contains a study of the application of well-known deconvolution techniques to passive radar data. The work in [3, 4] proposes the use of time-frequency distributions for passive radar imaging. Finally, [5] contains a derivation of Cramér-Rao bounds for target shape estimation in passive radar.

Television and FM radio broadcasts operate at wavelengths that are much larger than those typically employed in active radar imaging systems. For instance, an X-band radar might operate at 10 GHz, whereas a passive radar system operates in the VHF and UHF bands (55-885 MHz). From an imaging viewpoint, lower frequencies result in reduced cross-range resolution; hence, to achieve high-resolution images, the target needs to be tracked for some length of time to obtain data over a wide range of angles. Another consequence is that low-frequency images contain extended features, and are not well-modeled by a small number of scattering centers. Furthermore, the signals involved in such broadcasts have much lower bandwidth than the signals used in active radar systems. As a result, given one transmitter-receiver pair, the achievable range resolution is very poor. Hence one needs to make use of multiple transmitters for reasonable coverage in the spatial spectrum.

As a result of these constraints and requirements, forming images of aircraft using passive radar systems involves reconstructing an image from sparse and irregular samples of its Fourier transform [2,6]. The sampling pattern in a particular data collection scenario depends on the locations of the transmitters and the receiver, as well as the flight path of the object to be imaged; hence it is highly variable. Conventional Fourier transform-based imaging essentially sets the unavailable (due to the sparse aperture) data samples to zeros. This results in various artifacts in the formed image, the severity of which depends on the

specifics of the data collection scenario.

Motivated by the limitations of direct Fourier transform-based imaging in the context of passive radar, an alternative idea of using a deconvolution technique borrowed from radio astronomy (namely the CLEAN algorithm [7, 8]) has been explored in [2]. However, the results of the study in [2], summarized in Sec. IV-D, suggest that the CLEAN algorithm does not outperform direct Fourier reconstruction for passive radar imaging, due to the following reasons. The CLEAN algorithm, as well as other deconvolution algorithms based on similar sparse image assumptions, work best on images that are well-modeled as a set of distinct point scatterers. Hence, such algorithms are well-suited to high-frequency imaging of man-made targets, as the current on the scatterer surface tends to collect at particular points. When using low frequencies of interest in passive radar, the images are more spatially distributed. In addition, the complex-valued, and potentially random-phase [9] nature of radar imaging also presents a complication for CLEAN. The complex-valued characteristics of both the underlying image and the observation model produce constructive and destructive interference effects that conspire to obscure true peaks in the underlying reflectance, causing them to be missed by the CLEAN algorithm, and more damagingly create spurious apparent peaks which mislead the algorithm.

To address these challenges, we adapt and use a recently-developed, optimization-based SAR imaging method [10]. This approach uses an explicit model of the particular data collection scenario. This model-based aspect provides significant reduction in the types of artifacts observed in conventional imaging. More importantly, the optimization framework contains non-quadratic constraints for region-based feature enhancement, which in turn results in accurate reconstruction of spatially-extended features. Finally, this approach explicitly deals with the complex-valued and potentially random-phase nature of radar signals. We present experimental results on data obtained through electromagnetic simulations via the Fast Illinois Solver Code (FISC), demonstrating the effectiveness of the proposed approach for passive radar imaging.

The remainder of this paper is organized as follows. Section II contains a review of the data collection process in passive radar, focusing on the resulting challenges for imaging. In Section III, we present our approach to passive radar image reconstruction. Section IV

contains experimental results based on simulated data. In Section V, we discuss some of the limitations of the scope of the approach presented here, and suggest possible extensions for further exploration. Finally, Section VI concludes the paper.

II. DATA COLLECTION IN PASSIVE RADAR

In a bistatic radar, the transmitter and receiver are at different locations. The angle between the vector from the target to the transmitter and the vector from the target to the receiver, corresponding to the incident and observed directions of the signal, is called the bistatic angle β. For monostatic radar, the bistatic angle is 0°. Figure 1(a) illustrates the bistatic radar configuration. The complex-valued data collected at transmitting frequency f is a sample of the Fourier transform of the target reflectivity, and is equivalent to a monostatic measurement taken at the bisecting direction and at a frequency of $f\cos(\beta/2)$ [11,12]. In a polar coordinate system, the bisecting direction gives the azimuthal coordinate in Fourier space, and $(4\pi f/c)\cos(\beta/2)$ gives the radial coordinate, where c is the speed of light. As the receiver rotates away from the transmitter, the bistatic angle β increases and the equivalent frequency $f\cos(\beta/2)$ decreases. When β is 180°, the measurement is a sample located at the origin in Fourier space. Measurements collected from a receiver that rotates 360° around the target lie on a circle in Fourier space, passing through the origin. The diameter of the circle is $4\pi f/c$. Different incident frequencies give data on circles in Fourier space with different diameters, as shown in Figure 1(b). If the transmitter rotates around the target, the circle in Fourier space also rotates by the same amount and we get more circles of data in Fourier space. Figure 1(b) illustrates the type of Fourier space coverage obtained through angular and frequency diversity in a bistatic radar.

Unlike the case in active radar systems where one uses high-bandwidth signals, in passive radar based on radio and television signals, one is limited to much lower bandwidths. FM radio has a usable bandwidth of around 45 kHz, and although analog TV technically has a bandwidth of 6 MHz, little of that is usable for radar purposes. The synchronization (sync) pulses inherent in the analog TV signal result in extreme range ambiguities if one attempts traditional matched filtering range compression, as first discovered by Griffiths and Long in the mid-80s [13]. By the time the signal reaches the receiver, the only significant usable signal is the TV carrier itself, which contains around 50% of the total

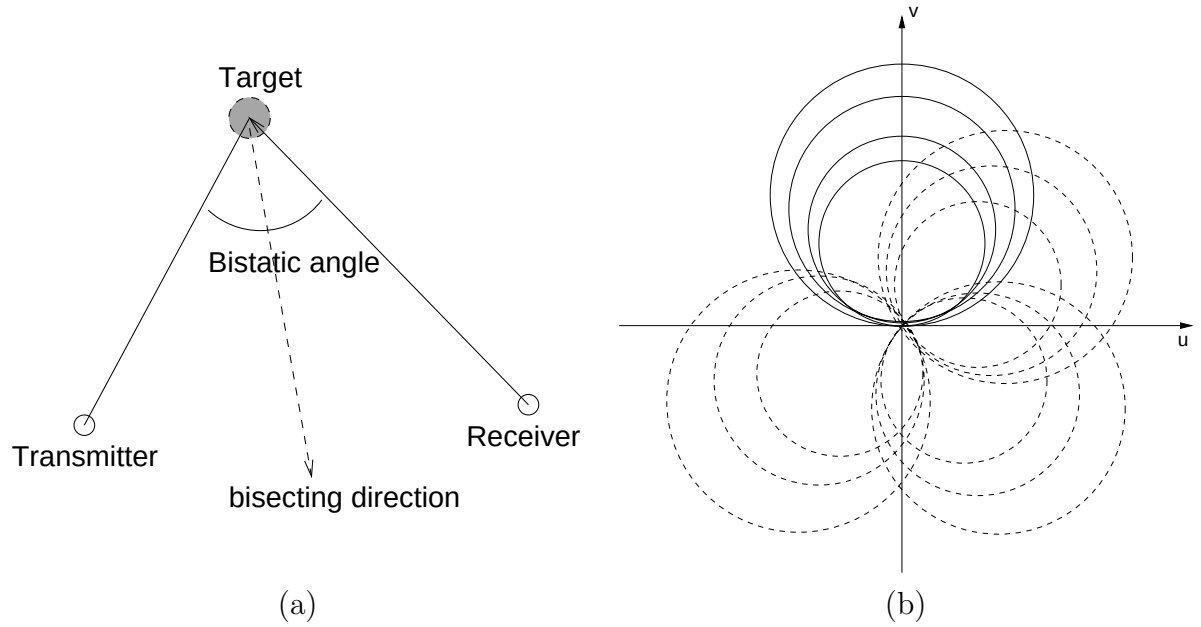

Fig. 1. (a) Bistatic radar configuration. (b) Bistatic Fourier space coverage due to angular and frequency diversity. The authors would like to thank Yong Wu, who created these figures for a DARPA annual report while a student at the Univ. of Illinois.

power[2] in the analog TV signal (see pp. 20-21 of [14]). We can essentially model the usable TV signal as a simple sinusoid. Consequently, at each observation instant, we might think of each transmitter-receiver pair providing essentially "one point" in the 2-D frequency spectrum. A multistatic system exploiting multiple television and radio stations should be used for obtaining the frequency diversity needed for reasonable-quality imaging. The bistatic imaging principle illustrated in Figure 1 applies to each transmitter/receiver pair in a multistatic system. The aircraft must be tracked and data collected over time to obtain angular diversity, with each transmitter-receiver pair providing data on an arc in 2-D Fourier space. Different transmitters use different frequencies and are at different locations, which leads to multiple arcs of Fourier data, providing further data diversity. In the passive radar scenario explored in this paper, there are multiple transmitters but just one receiver, although the basic idea could easily be expanded to include multiple receivers if appropriate data links are available.

[2]Having so much power in the carrier may seem wasteful from the standpoint of modern communications, but it should be remembered that at the time analog TV standards were developed, the receiver hardware had to be exceedingly simple. Essentially, the transmitter needs to provide its own "local oscillator" to the receiver.

In active synthetic aperture radar, either monostatic or bistatic, one conventional image formation technique is to interpolate the data to a rectangular grid, followed by an inverse Fourier transform. Fourier points outside of the available data support are simply set to zero. In monostatic SAR, this is called the polar format algorithm [15–17]. The bistatic version is similar, except the data is placed on the grid with the $\cos(\beta/2)$ warping described above [12, 17]. We can consider a similar approach as the "conventional" method for imaging in passive radar. In active monostatic radar imaging, the data in the spatial frequency domain usually lie in a regular annular region. The regularity of this region then leads to a sinc-like point spread function when the image is formed using a Fourier transform. On the other hand, in multistatic passive radar, the "sampling pattern" in the spatial frequency domain is much more irregular for a number of reasons. First of all, since the transmitted signals are narrowband, each transmitter-receiver pair provides a "point" rather than a "slice" of data. Secondly, to obtain reasonable azimuth resolution, data are collected over a wider range of observation angles. Thirdly, the look angles of different transmitter-receiver pairs lead to coverage in different areas of the spectrum. In a related fashion, where the data lie in the spectrum depends on the flight path of the object being imaged. As a result, when we form images using direct Fourier inversion, the imaging artifacts that we encounter are more severe than in the case of active radar systems. Furthermore, the nature of the artifacts cannot be determined just based on the system design, since the flight path of the aircraft has a role as well.

III. REGION-ENHANCED PASSIVE RADAR IMAGING

Based on the issues outlined in the previous section, we propose a different approach for passive radar imaging. Two main ingredients of this approach make it especially suited for passive radar applications. First, it is model-based, meaning that it explicitly uses a mathematical model of the particular observation process. As a result, it has a chance of preventing the types of artifacts that are caused by direct Fourier inversion. Second, it facilitates the incorporation of prior information or constraints about the nature of the scenes being imaged. This is important, since passive radar imaging is inherently an ill-posed problem. In particular, we focus on the prior information that at the low frequencies of interest in passive radar, the scenes contain spatially-extended structures, corresponding

to the actual contours of real aircraft. As a result, we incorporate constraints for preserving and enhancing *region-based* features, such as object contours.

The approach we use for passive radar imaging is based on the feature-enhanced image formation framework of [10], which is built upon non-quadratic optimization. This approach has previously been used in active synthetic aperture radar imaging. Let us provide a brief overview of feature-enhanced imaging, starting from the following assumed discrete model for the observation process:

$$\mathbf{g} = \mathbf{T}\mathbf{f} + \mathbf{w} \tag{1}$$

where $\mathbf{g}$ denotes the observed passive radar data, $\mathbf{f}$ is the unknown sampled reflectivity image, $\mathbf{w}$ is additive measurement noise, all column-stacked as vectors, and $\mathbf{T}$ is a complex-valued observation matrix. The data can be in the spatial frequency domain, in which case $\mathbf{T}$ would be an appropriate Fourier transform-type operator corresponding to the particular sampling pattern determined by the flight path of the target. Alternatively through a Fourier transform, one can bring the data into the spatial domain, and then use the resulting transformed observations as the input to the algorithm. In this case, $\mathbf{T}$ would be the point spread function corresponding to the particular data collection scenario. Our experiments are based on the latter setup.

The objective of image reconstruction is to obtain an estimate of $\mathbf{f}$ based on the data $\mathbf{g}$ in Eqn. (1). Feature-enhanced image reconstruction is achieved by solving an optimization problem of the following form:

$$\hat{\mathbf{f}} = \arg\min_{\mathbf{f}} \left\{ \|\mathbf{g} - \mathbf{T}\mathbf{f}\|_2^2 + \lambda_1 \|\mathbf{f}\|_p^p + \lambda_2 \|\nabla|\mathbf{f}|\|_p^p \right\} \tag{2}$$

where $\|\cdot\|_p$ denotes the ℓ_p-norm ($p \leq 1$), ∇ is a 2-D derivative operator, $|\mathbf{f}|$ denotes the vector of magnitudes of the complex-valued vector $\mathbf{f}$, and λ_1, λ_2 are scalar parameters. The first term in the objective function of Eqn. (2) is a data fidelity term. The second and third terms incorporate prior information regarding both the behavior of the field $\mathbf{f}$, and the nature of the features of interest in the resulting reconstructions. The optimization problem in Eqn. (2) can be solved by using an efficient iterative algorithm [10], based on half-quadratic regularization [18]. We describe a basic version of this algorithm in the Appendix.

Each of the last two terms in Eqn. (2) is aimed at enhancing a particular type of feature that is of importance for radar images. In particular, the term $\|\mathbf{f}\|_p^p$ is an energy-type constraint on the solution, and aims to suppress artifacts and increase the resolvability of *point* scatterers. The $\|\nabla|\mathbf{f}|\|_p^p$ term, on the other hand, aims to reduce variability in homogeneous *regions*, while preserving and enhancing region boundaries. The relative magnitudes of λ_1 and λ_2 determine the emphasis on such *point-based* versus *region-based* features. Therefore, this framework lets us reconstruct images with two different flavors: using a relatively large λ_1 yields *point-enhanced* imagery, and using a relatively large λ_2 yields *region-enhanced* imagery. In the context of passive radar imaging, our primary focus is to preserve and enhance the shapes of spatially-distributed objects. Hence, we emphasize the use of the region-enhancement terms here.

IV. EXPERIMENTS

A. Electromagnetic Simulation using FISC

Asymptotic codes such as XPATCH [19] do not work well for aircraft-sized targets at the low frequencies of interest in passive radar systems. Hence, the simulations in the remaining sections invoke the Fast Illinois Solver Code (FISC) [20, 21], which solves Maxwell's equations via the method of moments. FISC is extremely particular about the quality of CAD models it needs. In particular, FISC requires that each edge of each triangular facet exactly match the edge of some other triangular facet. The model must contain no internal or intersecting parts. Unfortunately, such models are rare; in particular, readily available models which are perfectly adequate for XPATCH are often not suitable for FISC.

Each experiment in this paper is conducted on two different targets: a VFY-218, and a Dassault Falcon 20. A FISC compatible model of the VFY-218 comes standard as part of the SAIC Champaign XPATCH/FISC distribution. For the Falcon 20, we started with a Falcon 100 model purchased from Viewpoint Datalabs (now called Digimation), which happened to be FISC compatible. The Falcon 20 is essentially a larger version of the Falcon 100, so we used an approximate Falcon 20 model (as done in [2]) by scaling the Falcon 100 model.

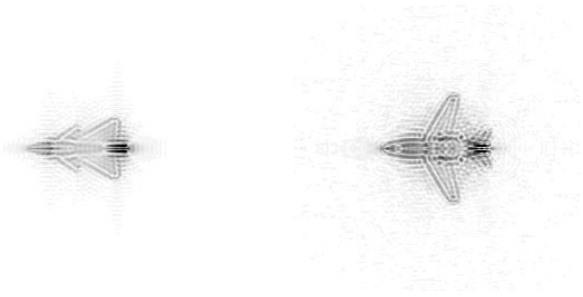

(a) (b)

Fig. 2. Reference passive radar images reconstructed from "full" datasets using direct Fourier reconstruction. The images are 256×256. (a) VFY-218. (b) Falcon 20.

Given such models, we construct Fourier datasets through FISC runs. In our experiments, we use only the HH-polarization data. The support of the data in the spatial frequency domain will in general be limited by the observation geometry and system parameters. However, to establish an "upper bound" on the expected imaging performance, let us first present the images we would obtain if we had a "full" dataset. To this end, let us use the Fourier data corresponding to 211.25 MHz (NTSC television channel 13) and incident and observed angles over the full 360 degree viewing circle. Such data would cover a disk in the spatial frequency domain [2]. The magnitudes of the radar images of the two targets, created by inverse Fourier transforming such data, are shown in Figure 2. Of course, such rich data sets would be unavailable in practice. However, these reconstructions can serve as "reference scenes" with which to compare the results of our experiments in the following sections, which are based on realistic data collection scenarios.

B. Experimental Setup

Figure 3 shows the locations of some high-power VHF television and FM radio stations in the Washington, DC area that are used in our simulations. The center of the coordinate system, where our hypothetical receiver is located, is the Lockheed Martin Mission Systems facility in Gaithersburg, Maryland. Five hypothetical flight paths are shown. The left column of Figure 4 shows the Fourier "sampling patterns" resulting from this particular transmitter/receiver geometry for each of the five flight paths. The sampling pattern indicates the support of the observed data in the spatial frequency domain for a particular flight path. Hence, the observed data for each flight path consists of a specific subset of

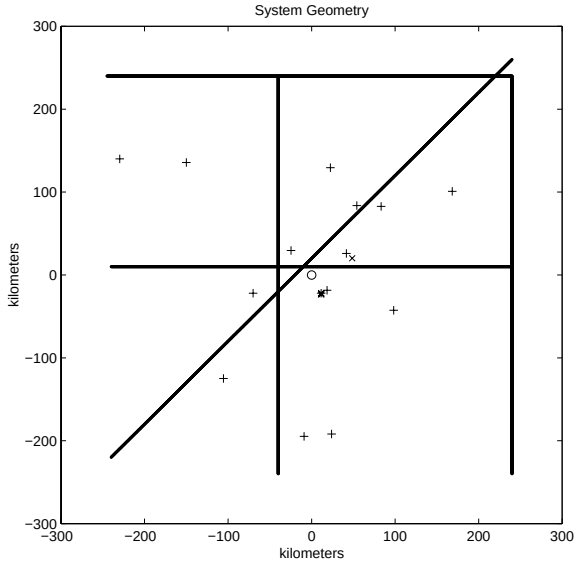

Fig. 3. Data collection geometry. VHF TV stations are represented with a ×; FM radio stations with a +; and the receiver with a circle. The lines represent five hypothetical flight paths.

the data used for reconstructing the images of Figure 2, whose contents are determined by the corresponding sampling pattern. The middle and right columns in Figure 4 show the magnitude of the corresponding point spread functions (PSFs) given by the inverse Fourier transform of the sampling patterns. The middle column shows magnitude on a linear scale, while the right column shows magnitude on a logarithmic scale to elucidate low-level detail in the sidelobes. Note that these sampling patterns, or equivalently PSFs, are used in specifying the observation matrix $\mathbf{T}$ in Eqn. (1). The next section presents results based on data associated with each of these flight paths.

C. Region-Enhanced Imaging Results

In all of the experiments presented here, for region-enhanced imaging we use $p = 1$ in Eqn. (2). For simplicity, we set $\lambda_1 = \lambda_2$ in all examples. This relative parameter choice appears to yield a region-enhanced image, together with suppression of some background artifacts. We choose the absolute values of these parameters based on subjective qualitative assessment of the formed imagery. Automatic selection of these parameters is an open research question. We do not specify the absolute values of λ_1 and λ_2 in the examples we present here, since those numbers are not that meaningful, as they depend on the scaling

of the data used.

Let us first consider the flight path corresponding to the sampling pattern in the bottom row in Figure 4. The corresponding "conventional" image of the VFY-218, obtained by direct Fourier transformation of the data, is shown in the top row of Figure 5(a). Points in the spatial frequency domain where observations are unavailable are set to zero. This is equivalent to convolving the reference image in Figure 2(a) with the PSF in the bottom row of Figure 4. As compared to the "reference" image of Figure 2(a), the direct Fourier reconstruction in the top row of Figure 5(a) contains severe imaging artifacts, resulting in suppression of some of the characteristic features of the imaged object. In this example we have not added any noise to the measurements. Hence, in the context of the observation model in Eqn. (1), we do not have any measurement noise. As a result, one can consider applying the pseudoinverse of the observation matrix, namely $\mathbf{T}^{\dagger}$, to the data to obtain a reconstruction $\hat{\mathbf{f}}_{\mathrm{PINV}} = \mathbf{T}^{\dagger}\mathbf{g}$. The pseudoinverse reconstruction obtained in this manner is shown in the top row of Figure 5(b). The region-enhanced reconstruction is shown in the top row of Figure 5(c). Both the pseudoinverse and the region-enhanced reconstructions provide reasonable results in this noise-free case, with the region-enhanced reconstruction providing somewhat better suppression of sidelobe artifacts. It is well-known that pseudoinverse solutions are very sensitive to noise, especially when the observation model results in an ill-conditioned matrix. The bottom row of Figure 5 shows the direct Fourier, the pseudoinverse, and the region-enhanced reconstructions, when we have a small amount of measurement noise.[3] The pseudoinverse solution breaks down in this case, and is in general useless in practical scenarios where observation noise is inevitable. The region-enhanced reconstruction exhibits robustness to noise, and preserves the characteristic features and shape of the VFY-218, despite the noisy sparse-aperture observations.

Let us now consider all the flight paths in Figure 4. In Figure 6, we show the reconstructions for the VFY-218. In columns (a) and (b), we have a small amount of measurement noise, resulting in a signal-to-noise ratio (SNR) of 30 dB.[4] Figure 6(a) and Figure 6(b)

[3]In these experiments we have added the noise after bringing the data to the spatial domain. Ideally, measurement noise should be added to the phase histories. However, we do not expect that to have any noticeable effect on our results.

[4]This should be interpreted as an average SNR, since data points may differ in power, yet the measurement noise on each data point has the same variance.

contain the direct Fourier, and the region-enhanced images, respectively. There is a row-to-row correspondence between Figure 4 and Figure 6, in terms of the flight paths. We observe that region-enhanced imaging produces reconstructions that preserve the features of the reference image of Figure 2(a) in a much more reliable way than direct Fourier imaging. In columns (a) and (b) of Figure 7, we show our results for the Falcon 20, again with data having an SNR of 30 dB, where we can make similar observations to the VFY-218 case. In columns (c) and (d) of Figures 6 and 7, we show reconstructions of the VFY-218 and the Falcon 20 respectively, for a noisier scenario where SNR = 10 dB. Region-enhanced imaging appears to produce reasonable results in this case as well.

We also observe that the direct Fourier images in the bottom three rows of Figures 6 and 7, while blurry, are clearer than the images in the top two rows. Looking at the corresponding sampling patterns in Figure 4, the primary difference seems to be that the paths corresponding to the top two rows keep the receiver and the transmitters on the same side of the target, yielding a quasi-monostatic (small bistatic angle) geometry, whereas in the bottom three rows, the target flies between the receiver and some of the transmitters, yielding large bistatic angles and wider effective coverage in frequency space. There are two important notes here:

1. The nature of the artifacts that may be caused by direct Fourier imaging depends on the flight path of the target being imaged, and hence may not be easily predicted prior to data collection. On the other hand, in Figures 6 and 7 we observe that region-enhanced images corresponding to different flight paths are much more similar to each other.

2. The paths where the target crosses between the transmitter and receiver, which give the best performance with conventional direct Fourier reconstruction in our simple simulation as shown in the bottom three rows of Figures 6, and 7, would be extraordinarily difficult to make work in practice. The direct signal from the transmitter is orders of magnitude larger than the reflected path. Passive radar systems usually alleviate this problem by placing the transmitter in an antenna null (either due to the physical shape of the antenna, or using adaptive nulling techniques in the case of an electronically beamformed array), and maybe also employing some additional RF cancellation techniques. Even with such techniques, the dynamic range requirements are stressing. It would be quite challenging to

simultaneously null the direct path signal and receive the reflected signal from an aircraft that is close to the transmitter in angle. For most practical systems, it would be desirable to stick with the quasi-monostatic "over the shoulder" geometry exemplified by the top two rows of Figures 4, 6, and 7. Therefore, it is important to have a technique like region-enhanced imaging, which can generate reasonable images in such quasi-monostatic scenarios.

On a laptop PC with a 1.80 GHz Intel Pentium-4 processor, the average computation time for the region-enhanced images presented (each composed of 256×256 pixels) was around 100 seconds, using non-optimized MATLAB code.

Finally, let us test the robustness of this image formation technique to an extreme amount of measurement noise. In Figure 8, we consider a scenario where SNR = -10 dB, and for the sake of space, we consider only one of the objects, namely the VFY-218, and only one of the flight paths, namely the one in the bottom row of Figure 4. The conventional image in Figure 8(a) is dominated by noise artifacts. On the other hand, the region-enhanced image in Figure 8(b) preserves the basic shape of the aircraft, despite some degradation in the image due to noise.

D. Experiments with CLEAN

To illustrate the need for a sophisticated technique like the region-enhanced approach used in the previous section, we conclude our experiments with some results using a simple CLEAN algorithm [7]. In the CLEAN algorithm, one finds the point with the largest magnitude in the "dirty map" (i.e. the conventional direct Fourier transform reconstruction) to be CLEANed, shifts the PSF of the system to that point, and normalizes the PSF so that its origin equals the value of the image at the found peak multiplied by a parameter called the *loop gain*. This shifted and normalized PSF is subtracted from the dirty map. A single point, corresponding to where the peak was in the dirty map, is added to a "clean map" which is built up as the algorithm proceeds. The procedure is iterated until some stopping criterion is met.

Figure 9 shows the results[5] of 400 iterations of the CLEAN algorithm on the VFY-218

[5]The raw CLEAN images are sparse and may be difficult to reproduce in print in their original state. Hence, the magnitudes of the radar images have been blurred by a Gaussian kernel, and the images are displayed on a

and the Falcon 20, based on noiseless data. We use a loop gain of 0.15, which has been a typical choice in radio astronomy applications of CLEAN. Again, there is a row-to-row correspondence between Figure 9 and Figure 4, in terms of the flight paths. These results should be compared to those of direct Fourier reconstruction and region-enhanced imaging in Figures 6 and 7. Although CLEAN has excelled in a number of high-resolution imaging scenarios, it does not seem to outperform standard direct Fourier reconstruction in the context of passive radar imaging. On the other hand, region-enhanced imaging appears to provide significantly improved imagery as compared to both Fourier reconstruction and CLEAN.

V. LIMITATIONS AND POSSIBLE EXTENSIONS

In this paper, we have assumed that the direct signal from the transmitter is available to provide a phase reference for the reflected signal from the target. More problematically, we have assumed that we know the passive radar observation model exactly, which involves knowledge about not only the transmitters and the receiver, but also about the flight path of the target being imaged. In practice, information about the target flight path is obtained from a tracking system, and will contain uncertainties. The uncertainties in the estimated path will be manifest as phase errors in the data. Considering that the phase of the Fourier transform of an image contains significant information, it is important to develop image formation techniques that can deal with such uncertainties in the observation model. The SAR community refers to such techniques as autofocus algorithms [17, 22]. Such an extension of the image formation technique we presented constitutes a challenging direction for future work. Maneuvering targets that may be rolling, pitching, and yawing in complex ways would present further challenges, even if the target positions over time were exactly known.

Our imaging model assumes isotropic point scattering. However, when the imaged object is observed over a wide range of angles, the aspect-dependent amplitude of scattering returns can become significant. Performing region-enhanced passive radar imaging under aspect and/or frequency-dependent anisotropic scattering would be an interesting extension of our work. Along these lines, the use of time-frequency transforms for wide-angle

square-root scale to make sure that faint features appear after copying.

imaging, motivated by the passive radar application, is discussed in [3], although the authors of [3] do not explicitly discuss how to address sparse apertures.

Our final remark is on frequency-dependent scattering. The tomographic radar model [12, 16] suggests that bistatic data at one frequency can be used to synthesize data at multiple lower frequencies. This assumption of frequency-independent scattering was employed in two places in our paper. It was used both in the construction of the observation model, and also in the creation of the simulated data. Since FISC runs are computationally expensive, we took advantage of this assumption and conducted a single run at 211.25 MHz. The fidelity of our simulations could be improved by conducting appropriate separate FISC runs for all the transmitters employed, even if no changes are made to the model used to form images from the data. A good avenue for future work would be to find out how far one could push the underlying bistatic equivalence theorems [23–25] in simulating data, before the disadvantage of lost accuracy due to frequency-dependent scattering exceeds the advantage of shorter computation times.

VI. CONCLUSION

We have explored the use of an optimization-based, region-enhanced image formation technique for the sparse-aperture passive radar imaging problem. Due to the sparse and irregular pattern of the observations in the spatial frequency domain, conventional direct Fourier transform-based imaging from passive radar data leads to unsatisfactory results, where artifacts are produced and characteristic features of the imaged objects are suppressed. The region-enhanced imaging approach we use appears to be suited to the passive radar imaging problem for a number of reasons. First, due to its model-based nature, the types of artifacts caused by conventional imaging are avoided. Second, it leads to the preservation and enhancement of spatially-extended object features. Third, unlike a number of deconvolution techniques, it can deal with the complex-valued nature of the signals involved. Our experimental results based on data obtained through electromagnetic simulations demonstrate the effectiveness and promise of this approach for passive radar imaging.

Appendix

Numerical Algorithm for Region-Enhanced Imaging

To find a local minimum of the optimization problem in Eqn. (2), we use a basic version of the numerical algorithm proposed in [10]. This algorithm is based on ideas from half-quadratic regularization [18], and can be shown to yield a quasi-Newton scheme with a special Hessian approximation. The algorithm is convergent in terms of the cost functional. In this Appendix, we only present the most basic form of this algorithm. Our goal here is only to provide a recipe for implementation, rather than a discussion of the properties of this numerical scheme.

To avoid problems due to non-differentiability of the ℓ_p-norm around the origin when $p \leq 1$, we use the following smooth approximation to the ℓ_p-norm in Eqn. (2):

$$\|\mathbf{z}\|_p^p \approx \sum_{i=1}^{K} (|(\mathbf{z})_i|^2 + \epsilon)^{p/2} \tag{3}$$

where $\epsilon \geq 0$ is a small constant, K is the length of the complex vector $\mathbf{z}$, and $(\mathbf{z})_i$ denotes its i-th element. For numerical purposes, we thus solve the following slightly modified optimization problem:

$$\hat{\mathbf{f}} \;=\; \arg\min_{\mathbf{f}} \left\{ \|\mathbf{g} - \mathbf{T}\mathbf{f}\|_2^2 + \lambda_1 \sum_{i=1}^{N} \left(|(\mathbf{f})_i|^2 + \epsilon\right)^{p/2} + \lambda_2 \sum_{i=1}^{M} (|(\nabla|\mathbf{f}|)_i|^2 + \epsilon)^{p/2} \right\}. \tag{4}$$

Note that we recover the original problem in Eqn. (2) as $\epsilon \to 0$. The stationary points of the cost functional in Eqn. (4) satisfy:

$$\mathbf{H}(\mathbf{f})\mathbf{f} = \mathbf{T}^H \mathbf{g} \tag{5}$$

where:

$$\mathbf{H}(\mathbf{f}) \triangleq \mathbf{T}^H\mathbf{T} + \lambda_1 \mathbf{\Lambda}_1(\mathbf{f}) + \lambda_2 \mathbf{\Phi}^H(\mathbf{f}) \nabla^T \mathbf{\Lambda}_2(\mathbf{f}) \nabla \mathbf{\Phi}(f) \tag{6}$$

$$\begin{aligned}
\mathbf{\Lambda}_1(\mathbf{f}) &\triangleq \operatorname{diag}\left\{ \frac{p/2}{(|(\mathbf{f})_i|^2 + \epsilon)^{1-p/2}} \right\} \\
\mathbf{\Lambda}_2(\mathbf{f}) &\triangleq \operatorname{diag}\left\{ \frac{p/2}{(|(\nabla|\mathbf{f}|)_i|^2 + \epsilon)^{1-p/2}} \right\} \\
\mathbf{\Phi}(\mathbf{f}) &\triangleq \operatorname{diag}\left\{ \exp(-j\phi[(\mathbf{f})_i]) \right\}
\end{aligned}$$

Here $\phi[(\mathbf{f})_i]$ denotes the phase of the complex number $(\mathbf{f})_i$, $(\cdot)^H$ denotes the Hermitian of a matrix, and diag$\{\cdot\}$ is a diagonal matrix whose i-th diagonal element is given by the expression inside the brackets. Based on this observation, the most basic form of the numerical algorithm we use is as follows:

$$\mathbf{H}\left(\hat{\mathbf{f}}^{(n)}\right)\,\hat{\mathbf{f}}^{(n+1)} = \mathbf{T}^H\mathbf{g} \tag{7}$$

where n denotes the iteration number. We run the iteration in Eqn. (7) until $\|\hat{\mathbf{f}}^{(n+1)} - \hat{\mathbf{f}}^{(n)}\|_2^2 / \|\hat{\mathbf{f}}^{(n)}\|_2^2 < \delta$, where $\delta > 0$ is a small constant.

References

[1] L. M. Ehrman and A. D. Lanterman, "Automatic target recognition via passive radar, using precomputed radar cross sections and a coordinated flight model," *IEEE Trans. on Aerospace and Electronic Systems*, submitted in Nov. 2003.

[2] A. D. Lanterman and D. C. Munson, Jr., "Deconvolution techniques for passive radar imaging," in *Algorithms for Synthetic Aperture Radar Imagery IX*, E. G. Zelnio, Ed., Orlando, FL, USA, Apr. 2002, vol. 4727 of *Proc. SPIE*, pp. 166–177.

[3] A. D. Lanterman, D. C. Munson Jr., and Y. Wu, "Wide-angle radar imaging using time-frequency distributions," *IEE Proceedings Radar, Sonar, and Navigation*, vol. 150, no. 4, pp. 203–211, Aug. 2003.

[4] Y. Wu and D. C. Munson, Jr., "Multistatic passive radar imaging using the smoothed pseudo Wigner-Ville distribution," in *IEEE International Conference on Image Processing*, Oct. 2001, vol. 3, pp. 604–607.

[5] J. C. Ye, Y. Bresler, and P. Moulin, "Cramér-Rao bounds for 2-D target shape estimation in nonlinear inverse scattering problems with application to passive radar," *IEEE Trans. Antennas and Propagation*, vol. 49, no. 5, pp. 771–783, May 2001.

[6] Y. Wu and D. C. Munson, Jr., "Multistatic synthetic aperture imaging of aircraft using reflected television signals," in *Algorithms for Synthetic Aperture Radar Imagery VIII*, E. G. Zelnio, Ed., Orlando, FL, USA, Apr. 2001, vol. 4382 of *Proc. SPIE*.

[7] J. Högbom, "Aperture synthesis with a non-regular distribution of interferometer baselines," *Astronomy and Astrophysics Supplement Series*, vol. 15, pp. 417–426, 1974.

[8] U. J. Schwarz, "Mathematical-statistical description of the iterative beam removing technique (method CLEAN)," *Astronomy and Astrophysics*, vol. 65, pp. 345–356, 1978.

[9] D. C. Munson Jr. and J. L. C. Sanz, "Image reconstruction from frequency-offset Fourier data," *Proc. IEEE*, vol. 72, no. 6, pp. 661–669, June 1984.

[10] M. Çetin and W. C. Karl, "Feature-enhanced synthetic aperture radar image formation based on nonquadratic regularization," *IEEE Trans. Image Processing*, vol. 10, no. 4, pp. 623–631, Apr. 2001.

[11] D. Mensa and G. Heidbreder, "Bistatic synthetic aperture radar imaging of rotating objects," *IEEE Trans. Aerosp. Electron. Syst.*, vol. 18, pp. 423–431, July 1992.

[12] O. Arıkan and D. C. Munson Jr., "A tomographic formulation of bistatic synthetic aperture radar," in *Proceedings of ComCon 88, Advances in Communications and Control Systems*, Oct. 1988.

[13] H.D. Griffiths and N.R.W. Long, "Television-based bistatic radar," *IEE Proceedings, Part F*, vol. 133, no. 7, pp. 649–657, December 1986.

[14] P.E. Howland, *Television Based Bistatic Radar*, University of Birmingham, England, 1997.

[15] J. Walker, "Range-Doppler imaging of rotating objects," *IEEE Trans. Aerosp. Electron. Syst.*, vol. AES-16, no. 1, pp. 23–52, Jan. 1980.

[16] D. C. Munson Jr., J. D. O'Brien, and W. K. Jenkins, "A tomographic formulation of spotlight-mode synthetic aperture radar," *Proc. IEEE*, vol. 71, pp. 917–925, Aug. 1983.

[17] C. V. Jakowatz Jr., D. E. Wahl, P. H. Eichel, D. C. Ghiglia, and P. A. Thompson, *Spotlight-mode Synthetic Aperture Radar: a Signal Processing Approach*, Kluwer Academic Publishers, Norwell, MA, 1996.

[18] D. Geman and G. Reynolds, "Constrained restoration and the recovery of discontinuities," *IEEE Trans. Pattern Anal. Machine Intell.*, vol. 14, no. 3, pp. 367–383, Mar. 1992.

[19] M. Hazlett, D. J. Andersh, S. W. Lee, H. Ling, and C. L. Yu, "XPATCH: a high-frequency electromagnetic scattering prediction code using shooting and bouncing rays," in *Targets and Backgrounds: Characterization and Representation*, W. R. Watkins and D. Clement, Eds., Orlando, FL, USA, Apr. 1995, vol. 2469 of *Proc. SPIE*, pp. 266–275.

[20] J. M. Song and W. C. Chew, "The Fast Illinois Solver Code: requirements and scaling properties," *IEEE Computational Science and Engineering*, vol. 5, no. 3, pp. 19–23, July-Sept. 1998.

[21] J. M. Song, C. C. Lu, W. C. Chew, and S. W. Lee, "Fast Illinois Solver Code (FISC)," *IEEE Antennas and Propagation Magazine*, vol. 40, no. 3, pp. 27–34, 1998.

[22] R. L. Morrison, "Entropy-based autofocus for synthetic aperture radar," M.S. thesis, Univ. of Illinois at Urbana-Champaign, 2002.

[23] J. I. Glaser, "Bistatic RCS of complex objects near forward scatter," *IEEE Trans. on Aerospace and Electronic Systems*, vol. 21, no. 1, pp. 70–78, Jan. 1985.

[24] J. I. Glaser, "Some results in the bistatic radar cross section (RCS) of complex objects," *Proc. of the IEEE*, vol. 77, no. 5, pp. 639–648, May 1989.

[25] R. L. Eigel, P. J. Collins, A. J. Terzouli, G. Nesti, and J. Fortuny, "Bistatic scattering characterization of complex objects," *IEEE Transactions on Geoscience and Remote Sensing*, vol. 38, no. 5, pp. 2078–2092, Sept. 2000.

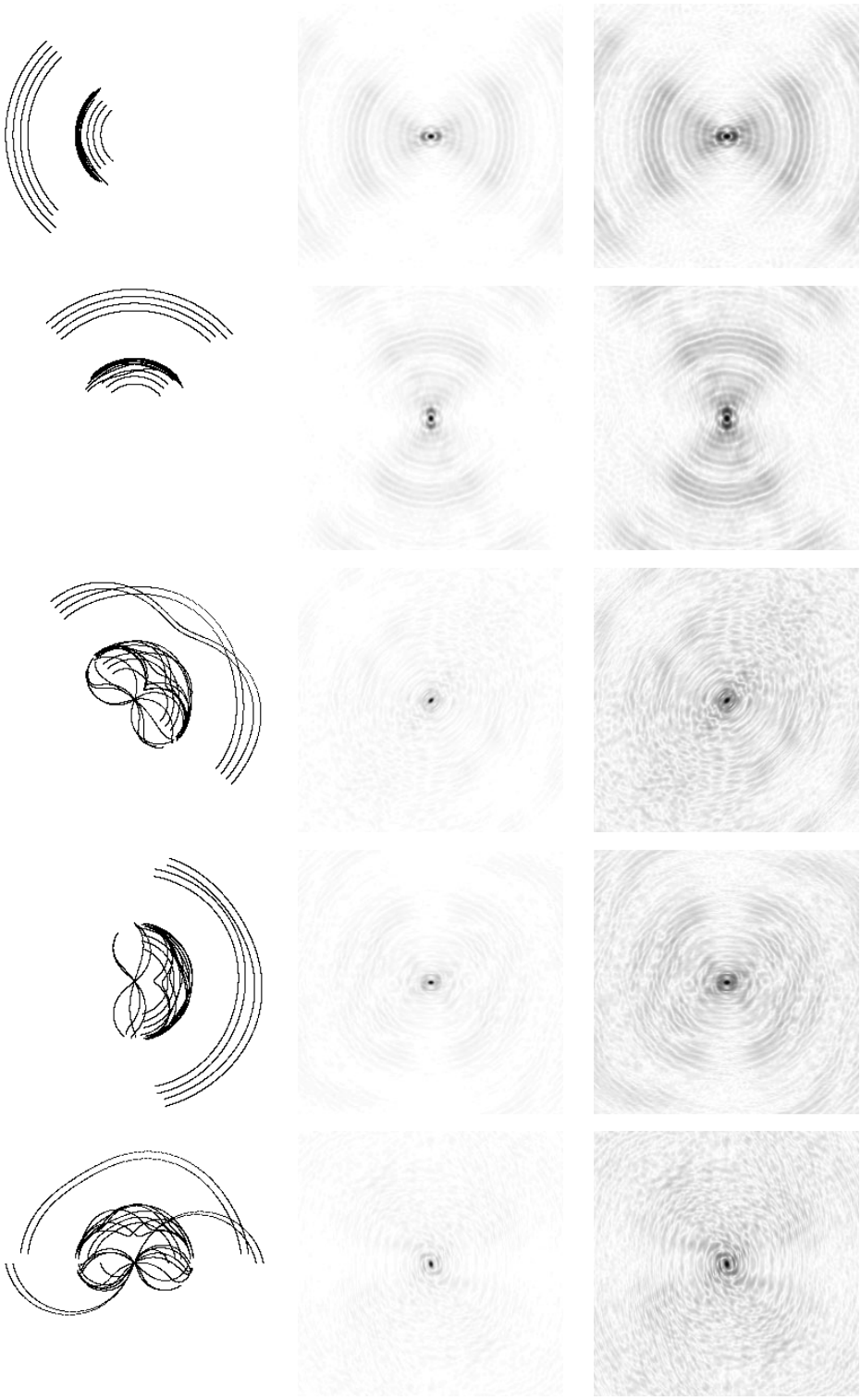

Fig. 4. Left column shows Fourier sampling patterns associated with five different flight paths. Remaining columns show the magnitude of the PSFs associated with the sampling patterns. The middle column uses a linear scale, while the right column uses a logarithmic scale to show fine detail. The PSFs are 256×256.

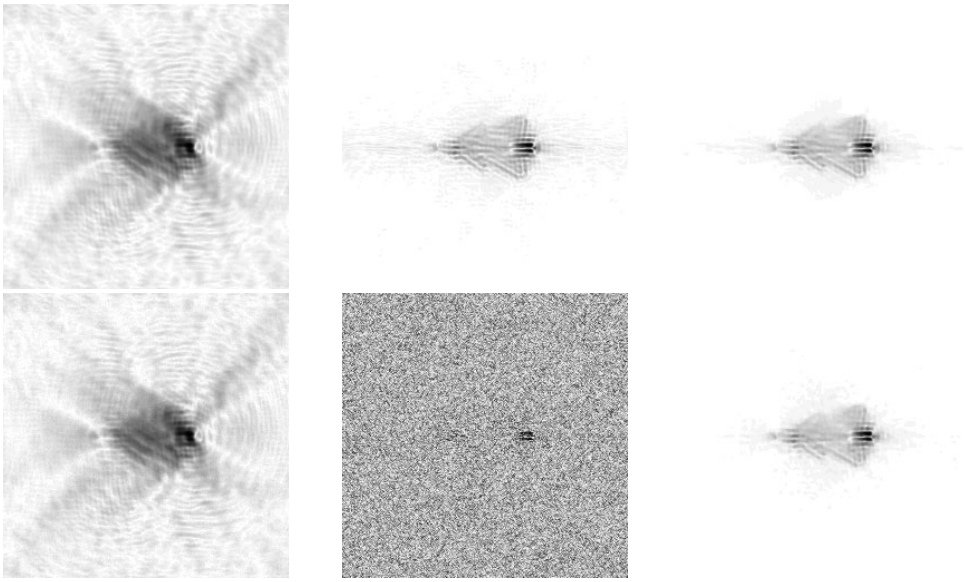

(a) (b) (c)

Fig. 5. Reconstructions of the VFY-218 based on data restricted to the Fourier sampling pattern shown in the bottom row of Figure 4. Top row: noiseless data. Bottom row: noisy data. (a) Direct Fourier reconstruction. (b) Pseudoinverse reconstruction. (c) Region-enhanced reconstruction.

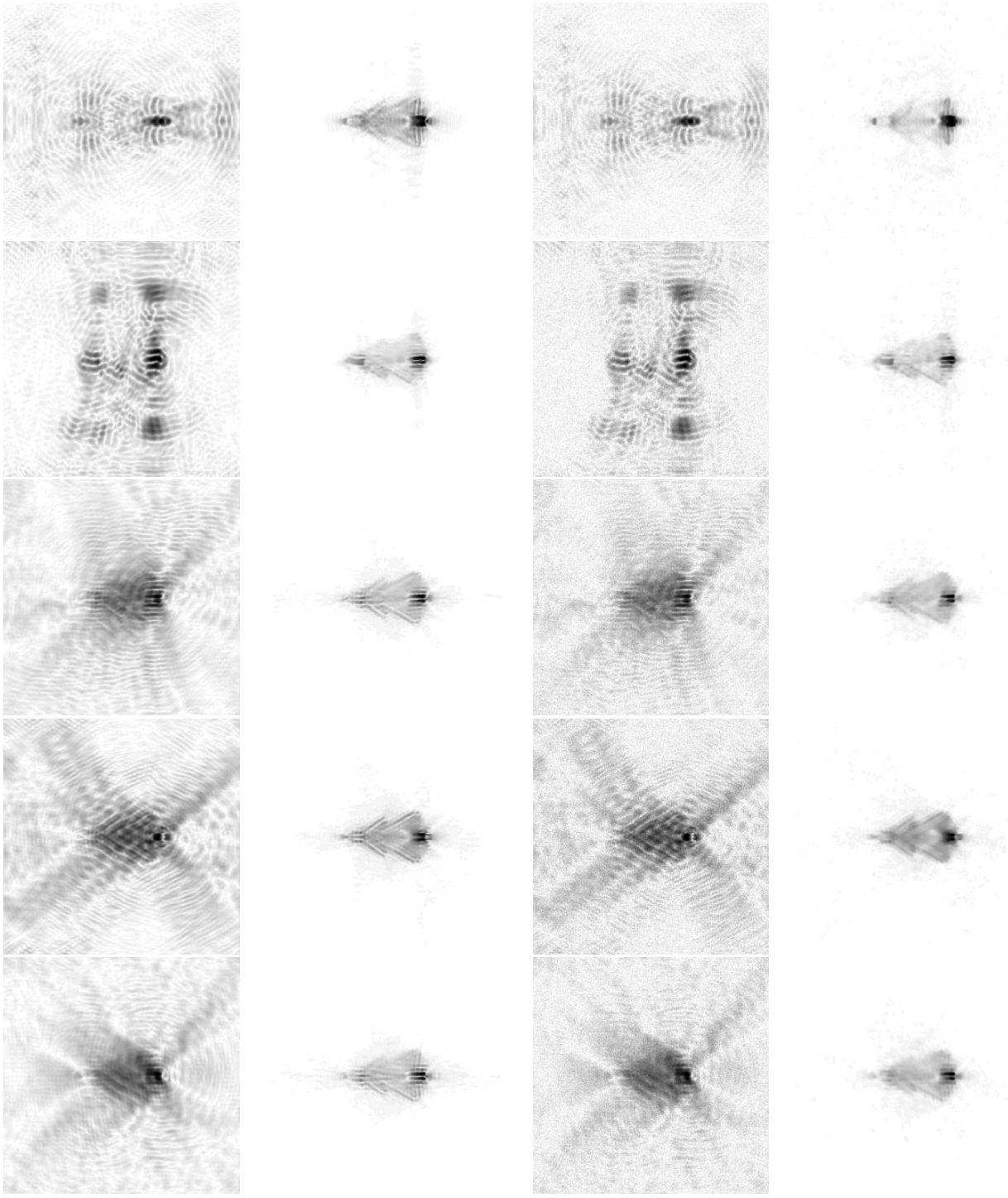

Fig. 6. Reconstructions of the VFY-218 based on data restricted to the Fourier sampling patterns shown in Figure 4. (a) Direct Fourier reconstructions, SNR = 30 dB. (b) Region-enhanced reconstructions, SNR = 30 dB. (c) Direct Fourier reconstructions, SNR = 10 dB. (b) Region-enhanced reconstructions, SNR = 10 dB.

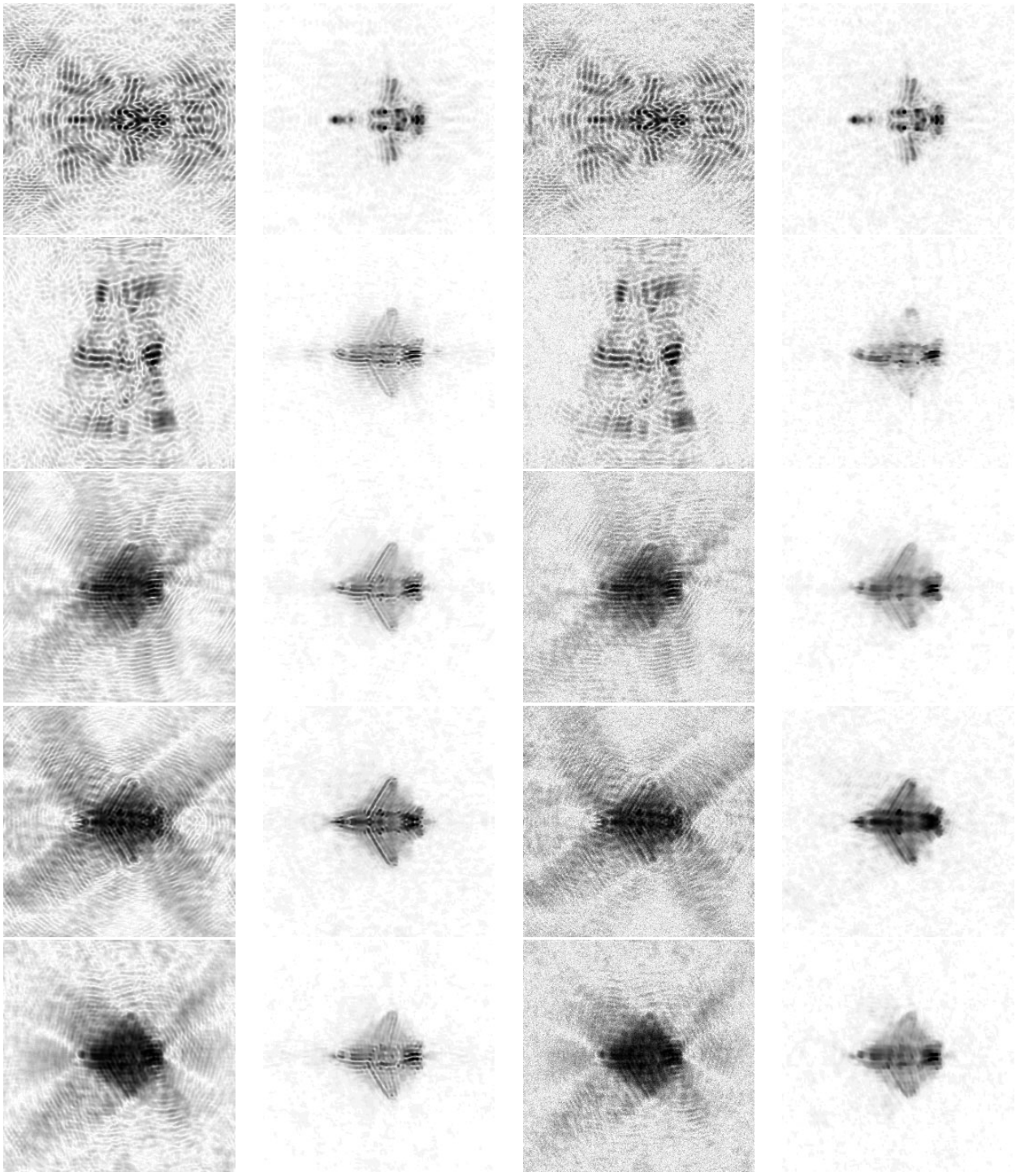

Fig. 7. Reconstructions of the Falcon 20 based on data restricted to the Fourier sampling patterns shown in Figure 4. (a) Direct Fourier reconstructions, SNR = 30 dB. (b) Region-enhanced reconstructions, SNR = 30 dB. (c) Direct Fourier reconstructions, SNR = 10 dB. (b) Region-enhanced reconstructions, SNR = 10 dB.

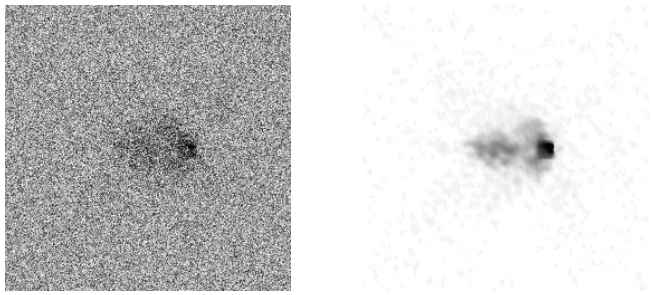

(a) (b)

Fig. 8. Reconstructions of the VFY-218 based on data (with SNR = -10 dB) restricted to the Fourier sampling pattern shown in the bottom row of Figure 4. (a) Direct Fourier reconstruction. (b) Region-enhanced reconstruction.

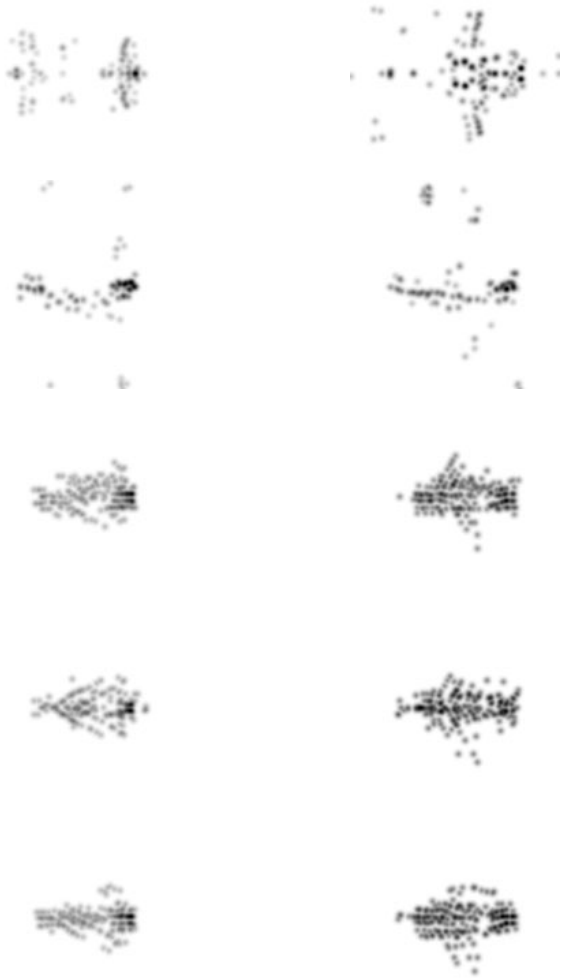

(a) (b)

Fig. 9. Results of 400 iterations of the CLEAN algorithm on noiseless data with a loop gain of 0.15. (a) VFY-218. (b) Falcon 20.